Article

Development of a Model for the Separation Characteristics of a Deflector Wheel Classifier Including Particle Collision and Rebound Behavior

Martin Weers [1,*], **Leonard Hansen** [1], **Daniel Schulz** [2], **Bernd Benker** [3], **Annett Wollmann** [1], **Carsten Kykal** [4], **Harald Kruggel-Emden** [2] and **Alfred P. Weber** [1]

1   Institute of Particle Technology, TU Clausthal, 38678 Clausthal-Zellerfeld, Germany;
    leonard.hansen@tu-clausthal.de (L.H.); annett.wollmann@tu-clausthal.de (A.W.);
    weber@mvt.tu-clausthal.de (A.P.W.)
2   Department of Mechanical Process Engineering and Solids, TU Berlin, 10623 Berlin, Germany;
    daniel.schulz@tu-berlin.de (D.S.); kruggel-emden@tu-berlin.de (H.K.-E.)
3   CUTEC Forschungszentrum, 38678 Clausthal-Zellerfeld, Germany; bernd.benker@cutec.de
4   TSI GmbH, 52068 Aachen, Germany; carsten.kykal@tsi.com
*   Correspondence: martin.weers@tu-clausthal.de; Tel.: +49-5323-72-3554

Abstract: Deflector wheel classifiers are widespread in industry for the separation of powders into fine and coarse powders. Even though this separation process has been known for quite some time, it is not yet fully understood, and existing models fail to precisely predict the separation characteristics. Due to the high throughput of deflector wheel classifiers, it is greatly beneficial to estimate the separation characteristics before the experiment. Here, the developed model critically examines the usual assumptions, such as ideal airflow, neglection of particle–wall and particle–particle interactions, or spherically-shaped particles. First, the investigation of the air flow using a Particle Image Velocimetry (PIV) system showed significant differences to the assumed ideal flow field, then particle sphericity and its influence on the interaction between the particles and the paddles of the deflector wheel was investigated and compared with particle rebound behavior on a static wall. Surprisingly, comminuted glass behaves similarly to comminuted limestone in multiple aspects and not like glass beads. To determine the number of particle–particle collisions, Discrete Element Method (DEM) simulations were performed. The aforementioned aspects found application in the model and the separation behavior was well-estimated.

Keywords: coefficient of restitution; deflector wheel classifier; DEM-Simulation; non-spherical particles; model; PIV

1. Introduction

Deflector wheel classifiers separate airborne particles into two fractions, i.e., fine and coarse particles. This dry separation process is widespread and particularly important for powders with high throughput requiring a tailored particle size distribution, such as cement or pigments. Particle motion in a deflector wheel classifier is based on the application of centrifugal force in a rotational airflow counteracted by the drag from air, flowing radially inwards between the rotating paddles [1]. Coarse particles are rejected to the outer edge of the deflector wheel, while fine particles follow the airflow through the deflector wheel and are later separated from the airflow by an aero cyclone [2–4].

The first separation models by Rumpf [1,5,6], Molerus [7,8], Schubert [9], and Husemann [10] describe the separation efficiency of a deflector wheel classifier based on geometrical and equilibrium considerations. To calculate the cut point (particle diameter at the split point between fine and coarse), these models consider the movement of single particles using multiple free coefficients to be determined from experiments.

Although it is of particular importance for the separation process, the flow field between the paddles was hardly considered for some time. With Laser Doppler Anemometer (LDA) measurements on a water model, Legenhausen [11] found that the flow between two separation paddles detaches, forming a flow vortex. A similar observation was made by Toneva et al. [12] using a combination of Particle Image Velocimetry (PIV) and Computational Fluid Dynamic (CFD) simulations [13]. Interestingly, Toneva et al. [13] found, in their numerical calculations, that the particles frequently collide with the separation paddles and that the coarse particles rebound in both backward and forward directions with respect to the airflow, thus, causing a deterioration of the separation sharpness [14,15].

A first approach to visualize particle movement in a deflector wheel classifier at high loadings with a high-speed camera was undertaken by Stender et al. [14]. They replaced the two-sided mounting of the wheel axis with a one-sided bearing and a glass panel, thus, obtaining direct optical access to the front side of the separator wheel. Next to the forming air vortices, they pointed out that particle–particle- and particle–wall-collisions affect the separation process [14,15]. A first approach to include particle–particle and particle–paddle collisions was performed by Spötter et al. [16], using an effective viscosity as a fitting parameter along the lines of the Richardson–Zaki model.

Here, a model is presented that tests and challenges the usual assumptions. At first, the air flow field in the paddle interspace is determined for this deflector wheel classifier by using a PIV system, then the focus is shifted to the particle behavior in the paddle interspace. For this new approach, the impaction and rebound characteristics for comminuted and spherical particles with different mechanical properties on different impaction plates were investigated in a systematic approach. The measurements in an impaction test bed are compared to measurements in the classifier. Additionally, the number of particle–particle collisions in the paddle interspace was determined by Discrete Element Method (DEM) simulations.

This article is organized in the following way. After the introduction, a short theoretical overview as a general basis for the later-described model is given. This includes the force equilibrium in the classifier, the effect of particle shape on the drag force, and impaction characteristics. After the methodology, the airflow between the paddles, the characteristics of the impaction events, and the DEM simulations are discussed in the results. Finally, these aspects found application in the described model to predict separation curves, which are then compared with measured ones.

2. Theoretical Basis for the Model Approach

The most basic approach to estimate the separation cut size is to consider spherical particles and a force balance at the outer edge of the classifier wheel between centrifugal force (Equation (1)) and drag force (Equation (2)) with the following assumptions: The particle tangential velocity is set equal to the deflector wheel circumferential velocity, and the cut size particle is defined as stationary in the radial direction, meaning $v_{rel} \approx v_{rad}$, where v_{rad} is the radial inward gas velocity between the paddles.

$$F_z = \rho_P V_P \frac{v_{\varphi,P}^2}{r} \tag{1}$$

$$F_D = c_D A_P \frac{\rho_{fl}}{2} |v_{rel}| v_{rel} \tag{2}$$

where ρ_P is the particle density, ρ_{fl} is the air density, V_P is the particle volume, $v_{\varphi,P}$ is the circumferential speed of the particle, r is the distance from the rotation axis, c_D is the drag coefficient, A_P iis the projection area of the particle, and v_{rel} is the relative velocity between the gas and the particle. The so obtained cut size in the Stokes flow regime is given in Equation (3), where η is the dynamic viscosity of air, ρ_P is the particle density, r_a is the

outer radius of the deflector wheel, $v_{rad(ra)}$ is the radial air velocity, and $v_{\varphi,P(ra)}$ is the particle tangential velocity at the outer radius of the deflector wheel, respectively [17,18].

$$x_{t,th} = \sqrt{\frac{18\eta}{\rho_P} \cdot r_a \cdot \frac{v_{rad\ (r_a)}}{v_{\varphi,P_{(r_a)}}^2}} \qquad (3)$$

The particle form significantly affects the separation curve for otherwise identical particles as shown in Figure 13b,c. While spherical glass particles show a sharp separation, the sharpness of cut decreases with increasing deviation from the spherical shape. Additionally, the expected cut points for the revolution rates, using the simple model of a force balance on the outer radius of the classifier, are indicated in Figure 13. Obviously, the measured cut sizes clearly differ from the simple model for non-spherical limestone particles.

2.1. Particle Sphericity

The particle shape directly affects multiple parameters of Equations (1) and (2). If a particle is less spherical, the surface area to volume ratio increases compared to spherical particles. A parameter often used to characterize this is the sphericity, which is unfortunately defined in various ways [19]. Additionally, a less spherically-shaped particle experiences more resistance in air, which can be traced back to the drag coefficient. Based on experiments and numerical studies, Hölzer and Sommerfeld [20] developed an expression for the drag coefficient, c_D, taking into account the particle Reynolds number, *Re*, and the 3D-sphericity, Ψ_{3D}, defined as the ratio of the surface area of the volume-equivalent sphere over the surface of the real particle (Equation (4)). The characteristic length in the particle Reynolds number is its volume-equivalent diameter. A distinction was made by considering the particle orientation about its movement. $\Psi_\perp$ is the cross-sectional area of a volume-equivalent sphere in relation to the particle cross-sectional area perpendicular to the flow. The parallel cross-section is used in the analog sphericity, $\Psi_\parallel$ [20]. The expression by Hölzer and Sommerfeld correlates very well with the particles used in their study, which were, for instance, cubes, octahedrons, and tetrahedrons.

$$c_D = \frac{8}{Re}\frac{1}{\sqrt{\Psi_\parallel}} + \frac{16}{Re}\frac{1}{\sqrt{\Psi_{3D}}} + \frac{3}{\sqrt{Re}}\frac{1}{\Psi_{3D}^{3/4}} + 0.42 \cdot 10^{0.4(-\log\Psi_{3D})^{0.2}}\frac{1}{\Psi_\perp} \qquad (4)$$

The particles used in this study do not show a strongly pronounced length to diameter ratio (cf. Figure 1). Therefore, no significant orientation effects are expected resulting in $\Psi_\perp = \Psi_\parallel$ in the averaged orientation. Using the theorem of Cauchy as a function between surface area and mean projection area, one can find $\Psi_{3D} = \Psi_\perp = \Psi_\parallel$.
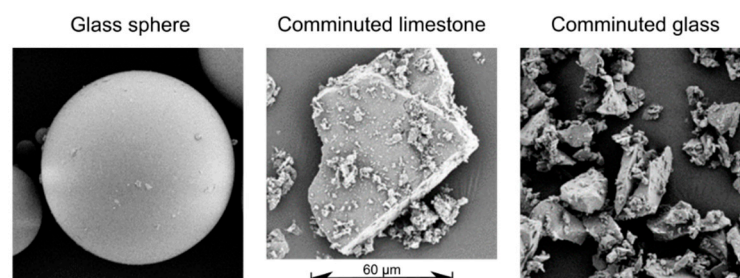

Figure 1. SEM images of the used materials showing a glass sphere (**left**), limestone particle (**center**), and comminuted glass (**right**). The scale applies to all images.

However, 3D sphericity is difficult to obtain. Only complex and expensive measurement systems can directly determine the 3D shape of randomly oriented particles in significant number and reasonable amount of time. Therefore, in the following the 2D sphericity, $\Psi_{2D,}$ is used as an approximation, i.e., the circumference of the area-equivalent

circle divided by the circumference of the particle projection area seen from a single direction. This measurement technique is widespread and the capture of a free moving particle's projection in bright field is far less complex than the 3D determination. For ground sand particles, Rorato et al. [19] found the following relation between Ψ_{3D} and Ψ_{2D} (Equation (5)), which has been validated in the range $0.5075 < \Psi_{3D} < 0.9998$.

$$\Psi_{3D} = 1.075\,\Psi_{2D} - 0.067 \tag{5}$$

Equation (6) concludes the aforementioned aspects to determine a volume-equivalent cut size $x_{V,t}$. Using the force balance between Equations (1) and (2), one needs to determine the ratio between particle volume and particle projection area. At first, the theorem of Cauchy substitutes the particle projection area, A_P with one-fourth of the particle surface, assuming that no concave surfaces are present. Then the 3D sphericity, Ψ_{3D}, gives the correlation between a particle's volume V_P and its surface. At last, the particle volume can be replaced by the volume-equivalent diameter $x_{V,t}$.

$$x_{V,t} = \frac{3 \cdot \rho_{fl}}{4 \cdot \rho_P} \cdot r \cdot \frac{v_{rad}^2}{v_{\varphi,P}^2} \cdot \frac{c_{D(Re,\Psi 3D)}}{\Psi_{3D}} \tag{6}$$

The range of the Reynolds number (*Re*) encountered in the present experiments reaches values up to almost 100. Therefore, Equation (4) for c_D in the transition regime cannot be simplified and must be solved iteratively. The resulting cut sizes are also presented in Figure 13, assuming the same parameters as for Equation (3) and are still very different from the experimental cut size, thus, indicating that in the classifier the effect of irregular particle shape goes far beyond a modified drag coefficient.

2.2. Impact/Collision Characteristics

Even more than the drag force, the impaction behavior is affected by particle form. An energy balance for particle–particle- and particle–wall-collision is quite tricky to resolve, even for spherical particles, since energy losses occur through several channels, such as plastic deformation, adhesive forces, and friction, resulting in local deformation, heat release, surface waves, and more. Even without losses, elastically stored, translational, and rotational energy are difficult to determine for a single impact. To avoid these problems, the coefficient of restitution (*COR*) is often employed in the literature [21–23] for overall description. This dimensionless quantity (see Equation (7)) is defined as the ratio of rebound ($v_{p,r}$) to impact particle velocity ($v_{p,i}$) with a stagnant wall. In case of a homogenous spherical particle impacting on a smooth wall, the *COR* can be predicted from the mechanical properties of the contact partners [24,25].

$$COR = \frac{v_{p,r}}{v_{p,i}} \tag{7}$$

The deflector wheel paddles move with the velocity, v_w, towards the incoming particles so that the relative normal velocities are $v_{p,rel,i} = v_{p,i} + v_w$ and $v_{p,rel,r} = v_{p,r} - v_w$ for impacting and rebounding particles, respectively. The values of the COR were measured with a high-speed camera for the particle impact with the rotating wheel and against a plate at rest ($v_w = 0\,\text{m/s}$). There are two types of restitution coefficients: normal and tangential. Because the deflector wheel velocity is much greater than the particle velocity, the normal COR was used in this study. The results determined by the stationary impaction wall and the spinning deflector wheel are consistent. As an extrapolation, it is assumed that the experimental COR data determined with a stationary wall can be applied for particle–particle collisions if both collision partners are of the same material. In this context, the stationary wall is understood as a particle with nearly infinite mass.

3. Materials and Methods

3.1. Material

The experiments were performed with glass beads (Glasperlen 0–50, Glasperlen 40–70, Samore, Bindlach, Germany), limestone (Saxolith 40, Saxolith 70, SH Minerals, Heidenheim, Germany), and ground glass particles.

Figure 1 shows Scanning Electron Microscope (SEM) micrographs of representatively selected particles. While the glass beads are predominantly ideal spheres, and the number of non-spherical particles is negligibly small, the comminuted particles show edges and corners. Their shape can better be described as tetrahedron or brick. The comminuted glass particles are smaller than the other two particulate materials, shown in Figure 2 (left). This figure displays the volume-weighted particle size distribution measured with a laser diffraction system (HELOS, Sympatec, Clausthal-Zellerfeld, Germany), while Figure 2 (right) shows the 2D sphericity of the comminuted materials, measured with a dynamic image analysis device (QICPIC, Sympatec). Here, the error bar corresponds to one standard deviation of each of the 10 µm intervals containing at least 1000 particles. In addition, the particles' Stokes number was calculated. This dimensionless quantity describes the follow-up behavior of the particle movements because of changing external conditions. The Stokes number is defined as the ratio of the stopping distance of the particle to a characteristic length, which in this case, is the blade front with 7 mm. For Stokes numbers much greater than one, the particle motion is unaffected by the gas motion, whereas for Stokes numbers much smaller than one, the particle motion perfectly follows the gas motion [26]. The materials being classified exhibit a stopping distance of at least 145 mm, resulting in a Stokes number of 20 or higher. This was calculated for "worst-case" particles with a diameter of approximately 20 µm at 15,000 rpm rotor speed (circumferential velocity at the outer radius ($v_{\varphi(ra)}$) = 39 ms^{-1}).
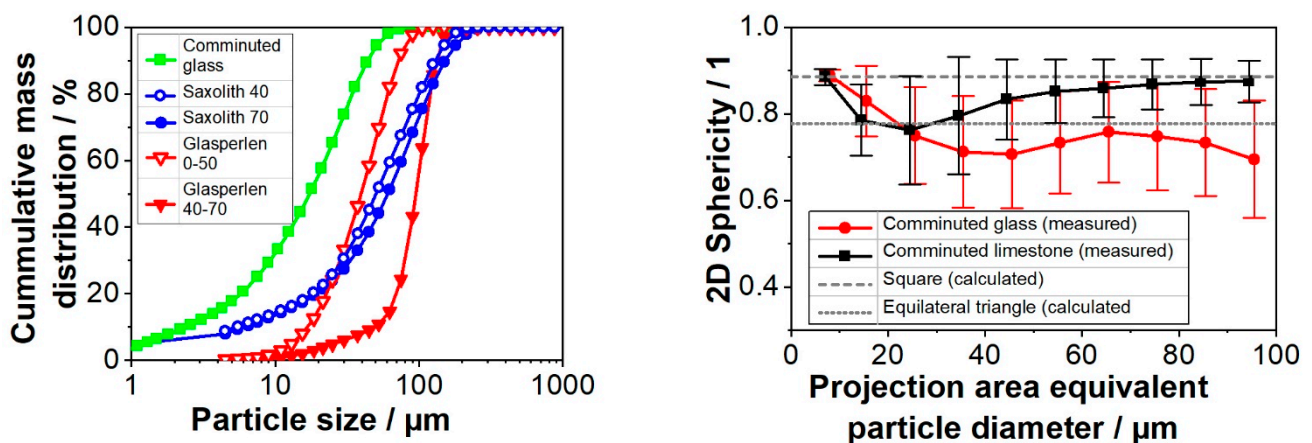

Figure 2. Particle size distributions of the used materials (**left**). "Saxolith" corresponds to the comminuted limestone and "Glasperlen" to the glass beads. The 2D sphericity of the comminuted materials is shown on the (**right**) side. The points are slightly offset, to enhance the visibility of the error bars, which indicate one standard deviation determined by a sample of at least 1000 particles per 10 µm size interval. The connecting line between the points is a guide for the eye.

3.2. Deflector Wheel Classifier

In this work, an ATP 50 deflector wheel classifier from Hosokawa Alpine (Augsburg, Germany), modified by Stender [14], is used (cf. Figure 3). While the standard ATP 50 uses a classifier wheel with a hollow shaft mounted on two sides, this classifier wheel is mounted only on one side and a glass disc closes the front side. Three optical access points are built into the housing.
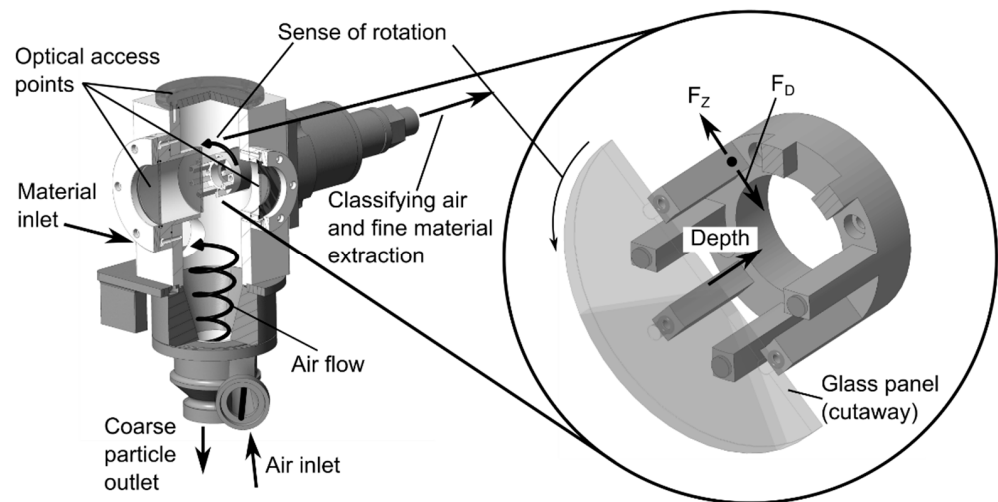
Figure 3. Deflector wheel classifier, basic principle, and modifications for optical access.

3.3. Particle Image Velocimetry (PIV) Measurements

The Particle Image Velocimetry (PIV) measurements were conducted with a commercial system from TSI. The camera was the model 630092 (8 MP CCD PIV Camera), together with a lens produced by Sigma (105 mm, 1:2.8, DG Macro). The laser sheet was generated with a laser (Quantel Evergreen, 200 mJ) and light-sheet optics with continuously adjustable focusing and a 25 mm cylinder lens (TSI, model 610026, Aachen, Germany). For synchronization and triggering of the PIV setup, the laser pulse synchronizer TSI, model 610036, was used. The camera, laser, and the deflector wheel shaft were synchronized using the signal from the revolution sensor (AV-ROS-W, Avibia, Engelskirchen, Germany).

During the measurements, the camera faced the front of the deflector wheel, while the laser created a light sheet orthogonal to the camera view (cf. Appendix A). Its position behind the glass cover of the deflector wheel ("depth") was 3 mm, 9 mm, and 15 mm, respectively. As tracer particles to visualize the gas flow, Aeroxide AluC (Evonik, Essen, Germany) was dispersed into the air inlet of the deflector wheel classifier by a dry powder dispersion unit (RODOS, Sympatec). The particles exhibited significant porosity (tamped density of 50 kg/m^3) with a mean particle size ($x_{50,3}$) of 5.8 µm. Using the deflector wheel front face as the characteristic length again, this resulted in a maximum Stokes number of 0.02 at a stopping distance of 0.17 mm.

Each set of pictures consisted of 200 pairs with an appropriate time spacing so that the particles in the region of interest were shifted by approximately 5 pixels.

In the preprocessing, first, a mean picture pair was generated to subtract from the series. In the following processing, a Recursive Nyquist Grid was used with a starting spot size of (256 pixels)^2 and a final spot size of (64 pixels)^2. In the post-processing, first, a global validation was used to eliminate vectors totally out of scope, and afterward, a local validation compared the found vectors with their neighbors. This led to between 15,000 and 50,000 accepted vectors for the different measurement positions.

3.4. Impact Characteristics Measured in the Impact Test Bed and the Classifier

The general setup and procedure for the particle impact characteristics have already been described in detail in [27]. Here, a brief overview of the settings and equipment that was used is given. The particles were placed in an acceleration tube with a slit as an outlet and a rubber hose closed on one side as an accelerator. The particles were shot onto a wall by stretching and releasing the rubber part. The impaction process was recorded in bright field illumination with a high-speed camera and a microscope lens. Due to 230,000 fps and the 50× magnification, particles as small as 20 µm could be recorded with a velocity of up to 50 m/s. A superimposed picture of the impaction process is shown in Appendix B. For the corresponding measurements of the particle trajectories in the deflector wheel classifier, an

additional macro-objective was used. The impact test bed offered several advantages, such as an easier comparison with the available literature data and a more precise investigation due to the improved magnification.

3.5. Discrete Element Method (DEM) Simulations

DEM simulations, similar to the one from [16], were performed for the gap between two adjacent deflector wheel paddles. This is also shown in the Supplementary Information in the form of a recording of the 3D simulation of the paddle interspace for polyhedral-shaped particles at 3000 rpm. As discussed later, the numerical approach was supported by dedicated experimental data, such as the actual mass loading [27], the average coefficient of restitution, the particle motion before impact with the deflector wheel, and the air flow field. The particle size distribution of "Saxolith 70" was used in the simulations for the feed material and additional parameters are given in Appendix D. In the DEM simulations, particles were tracked individually, while the particle/fluid force was one-way coupled with a stationary fluid field that was measured by the PIV system. The translational and rotational motion for non-spherical particles is obtained by integrating Newton and Euler equations of each particle given by:

$$m_i \frac{d^2 \vec{x}_i}{dt^2} = \vec{F}_i^{c} + \vec{F}_i^{pf} + \vec{F}_i^{z} + m_i \vec{g}, \tag{8}$$

$$\hat{I}_i \frac{d\vec{W}_i}{dt} + \vec{W}_i \times \left(\hat{I}_i \vec{W}_i \right) = \Lambda_i^{-1} \vec{M}_i, \tag{9}$$

with the particle mass (m_i,), particle acceleration ($d^2 \vec{x}_i / dt^2$), contact force ($\vec{F}_i^{c}$), which includes particle–particle and particle–wall contacts, particle/fluid force ($\vec{F}_i^{pf}$), centrifugal-force ($\vec{F}_i^{z}$), gravitational force ($m_i \vec{g}$), angular acceleration ($d\vec{W}_i / dt$), angular velocity, ($\vec{W}_i$), the external moment resulting out of contact or particle/fluid forces ($\vec{M}_i$), the inertia tensor along the principal axis ($\hat{I}_i$), and the rotation matrix converting a vector from the inertial into the body-fixed frame (Λ_i^{-1}). To save computing time and enable stationary walls (deflector wheel), the coordinate system rotates instead of the deflector wheel, which does not affect the simulation results, since the particle–wall contact is calculated with the relative velocity of particles and deflector wheel.

The particle/fluid force is calculated with the model of Di Felice [28], as this method is also suitable for non-spherical particles. The resulting combined drag and pressure gradient force reads as:

$$\vec{F}_i^{pf} = \frac{1}{2} \rho_f \left| \vec{v}_f - \vec{v}_i \right| c_D A_\perp \varepsilon_f^{1-\chi} \left(\vec{v}_f - \vec{v}_i \right) \tag{10}$$

$$\chi = 3.7 - 0.65 \exp\left(-(1.5 - \log(Re))^2 / 2 \right) \tag{11}$$

where ρ_f is the fluid density, $\vec{v}_f - \vec{v}_i$ is the relative velocity of fluid and particle i, c_D is the drag coefficient, $A_\perp$ is the cross-sectional area perpendicular to the flow, ε_f is the local fluid porosity, and χ is a correction factor, which is dependent on the particle Reynolds number Re. The model of Hölzer and Sommerfeld [20] is again used for the estimation of c_D (cf. Equation (4)), and the centrifugal force, $\vec{F}_i^{z}$, is calculated similar to Equation (1). The contact force, $\vec{F}_i^{c}$, as a result of particle–particle and particle–wall contacts is determined with a linear spring damper model for the normal component, corresponding to the experimentally determined normal restitution coefficient COR. The tangential component $\vec{F}_i^{t}$ is obtained using a linear spring limited by the Coulomb condition. A more detailed description of our numerical method can be found in our previous publications, e.g., [29].

4. Results and Discussion

In this work, the models of Spötter [30] and Weers [27] were further modified and optimized to predict the separation characteristics of a deflector wheel classifier for materials differing in morphology. As previously described, both are based on the particle entering the paddle interspace and undergoing the force equilibrium at different radii. The aim here was to better separate the material properties from the machine properties to gain a sound basis for a separation model that can be transferred to other systems with reasonable effort, such as one-point calibration, as described later. This section first shows the machine parameters' "airflow" and "particle approach" and then material parameters, such as the coefficient of restitution (COR). They are linked in the DEM to determine the number of particle–particle interactions. Finally, the model calculates separation curves based on the previously mentioned parameters.

4.1. Airflow Measured by PIV and the Resulting Deviation Factor

In contrast to very simple models (see e. g. Equation (3)), the whole flow, including the gaps between the classifier wheel paddles, is of cardinal importance for understanding particle separation. The vortex structure in these channels has already been described by [14,15,31,32] and others. The classifier geometries used by Sun et al. [32] and Xing et al. [31] differ significantly from the one used here and are, therefore, difficult to compare. Stender et al. [14] and Spötter et al. [15] studied the flow with a high-speed camera and tracer particles with a maximal Stokes number of 0.3. Their investigations found that at low rotational speeds, only a narrowing of the airflow exists, but at higher speeds, a full vortex is developed. In the present work, the Stokes number of the particles used as tracer for the gas motion was <0.02.

For the deflector wheel classifier used here, the central shaft inner radius is nearly as large as the inner radius of the deflector wheel paddles so that the classification process takes place between the paddles and not inside the potential vortex in the inner region of the wheel, as has been stated before [18,27].

Two dimensionless parameters are introduced here to make the measurement data for the different operating conditions more comparable. The circumferential deviation factor χ_ϕ and the radial deviation factor χ_{rad} compare the measured circumferential air velocity ($v_{\varphi,\,meas}$) (Equation (12)) or measured radial air velocity ($v_{rad,\,meas}$) (Equation (13)) to the usually assumed theoretical ones. The theoretical circumferential velocity ($v_{\varphi,\,wheel}$) is assumed to be the velocity of the deflector wheel at the corresponding radius, while the theoretical, inwardly directed radial velocity ($v_{rad,undisturbed}$) is calculated from the air volume flow (75 m^3 h^{-1}) and the open area to pass, assuming the deflector wheel does not spin. This ranges from 7.1 ms^{-1} to 11.9 ms^{-1} at the outer and inner radius of the deflector wheel, respectively.

$$deviation\ factor\ \chi_\varphi = \frac{v_{\varphi,\,meas}}{v_{\varphi,wheel}} \tag{12}$$

$$deviation\ factor\ \chi_{rad} = \frac{v_{rad,\,meas}}{v_{rad,\,undisturbed}} \tag{13}$$

Figure 4 shows the resulting 2D distribution of the deviation factor χ_ϕ for the tangential velocity between the deflector wheel paddles at three depth positions and three revolution rates. Each subplot consists of at least 500, 1000, and 1400 valid vectors for 3000, 9000, and 15,000 rpm, respectively (this also applies to Figure 5) measured in one paddle interspace. At the outer region of the deflector wheel, the tangential air velocity is mostly very slow and is in some cases oriented in the opposite direction. The tangential air velocity is always accelerated with a reducing radius and exceeds the deflector wheel velocity. While the deflector wheel paddles behave like a rigid body vortex with constant angular velocity, the air, on the other hand, conserves the angular momentum (potential vortex), leading to increased tangential velocity and deviation factors of up to 3.5. The only exception is in the measurements 3 mm behind the front glass panel at 9000 rpm

and 15,000 rpm. Here, wall effects might occur, reducing the acceleration. In most cases, the tangential air velocity is twice as fast as the deflector wheel at the inner radius of the paddles.
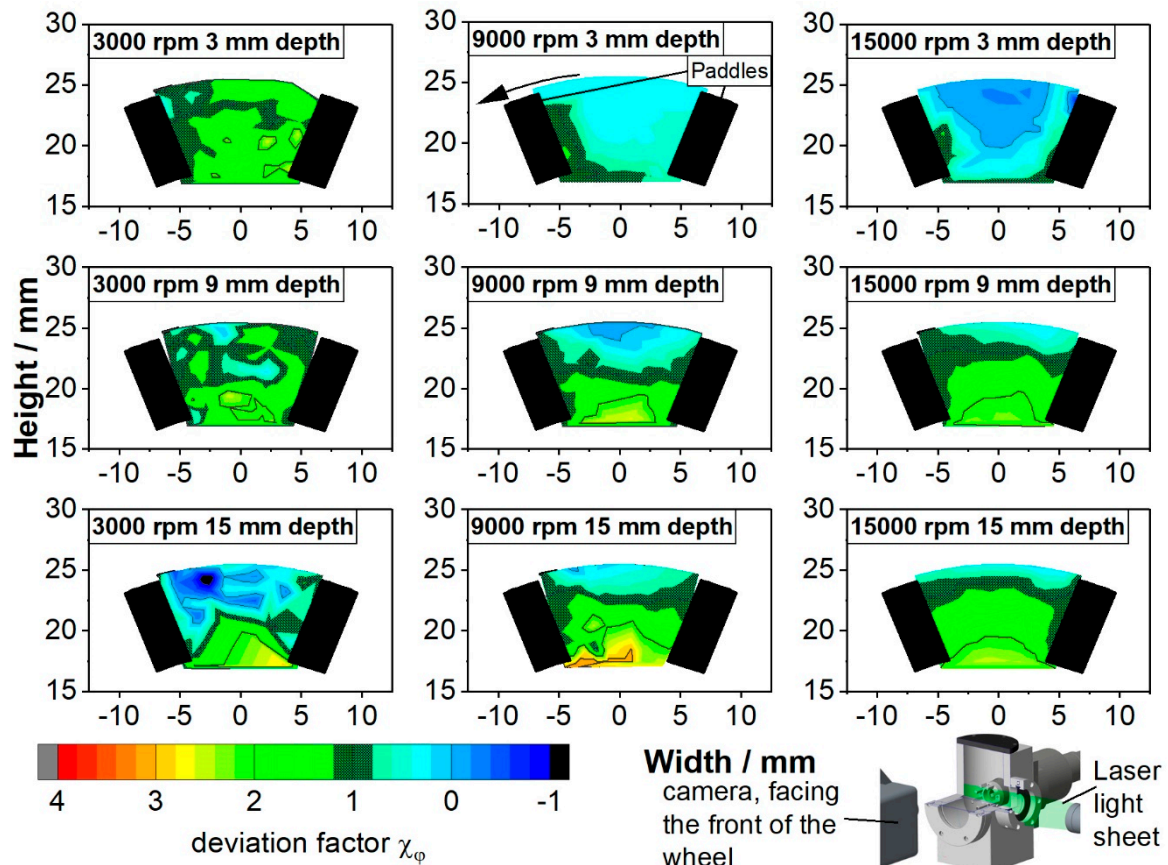

Figure 4. Measured tangential air velocity ($v_{\varphi,meas}$) divided by theoretically assumed $v_{\varphi,wheel}$ (deviation factor χ_ϕ) at different rotor speeds and depths behind the front glass panel. The black areas indicate the deflector wheel paddles, rotating counterclockwise. In the measurement, the laser light sheet was facing the side, while the camera faced the front. For better visibility, the result was turned by 90°. The black dotted region between the blades indicates a deviation factor χ_ϕ of $1 \pm 20\%$, meaning only for this small region the usually assumed tangential air velocity approximately equals the deflector wheel classifier velocity.

Figure 5 shows the measured radial air velocity divided by the assumed undisturbed one derived from mass balance and flow-through area (deviation factor χ_{rad}). Compared to Figure 4, it is obvious that the differences are more pronounced. The color bar here reaches from +4 to −4. At 15,000 rpm, the radial velocity still locally exceeds the color limits as indicated by a gray or black area, while at 3000 rpm, the area between the paddles is mainly filled with one color and slightly surpasses the assumed air velocity. Close to the leading paddle (left side), an inbound radial velocity was found, slower than expected from the undisturbed flow. This discrepancy gets much more pronounced with higher rotor speeds, leading to a strongly outbound flow (blue area).

Due to the inertia of the air, the rotation of the deflector wheel causes a high-pressure region in front of the trailing paddle and a low-pressure region behind the leading paddle. This results in increased radial velocity near the trailing paddle and, at best, decreased inward velocity near the leading paddle. An increased air velocity close to the tailing paddle means an increased drag force pointing inwards, thus, causing smaller cut sizes. So, if only the air flow is considered, the estimation of the cut size by Equation (3) or Equation (6) is coarser, i.e., worse.
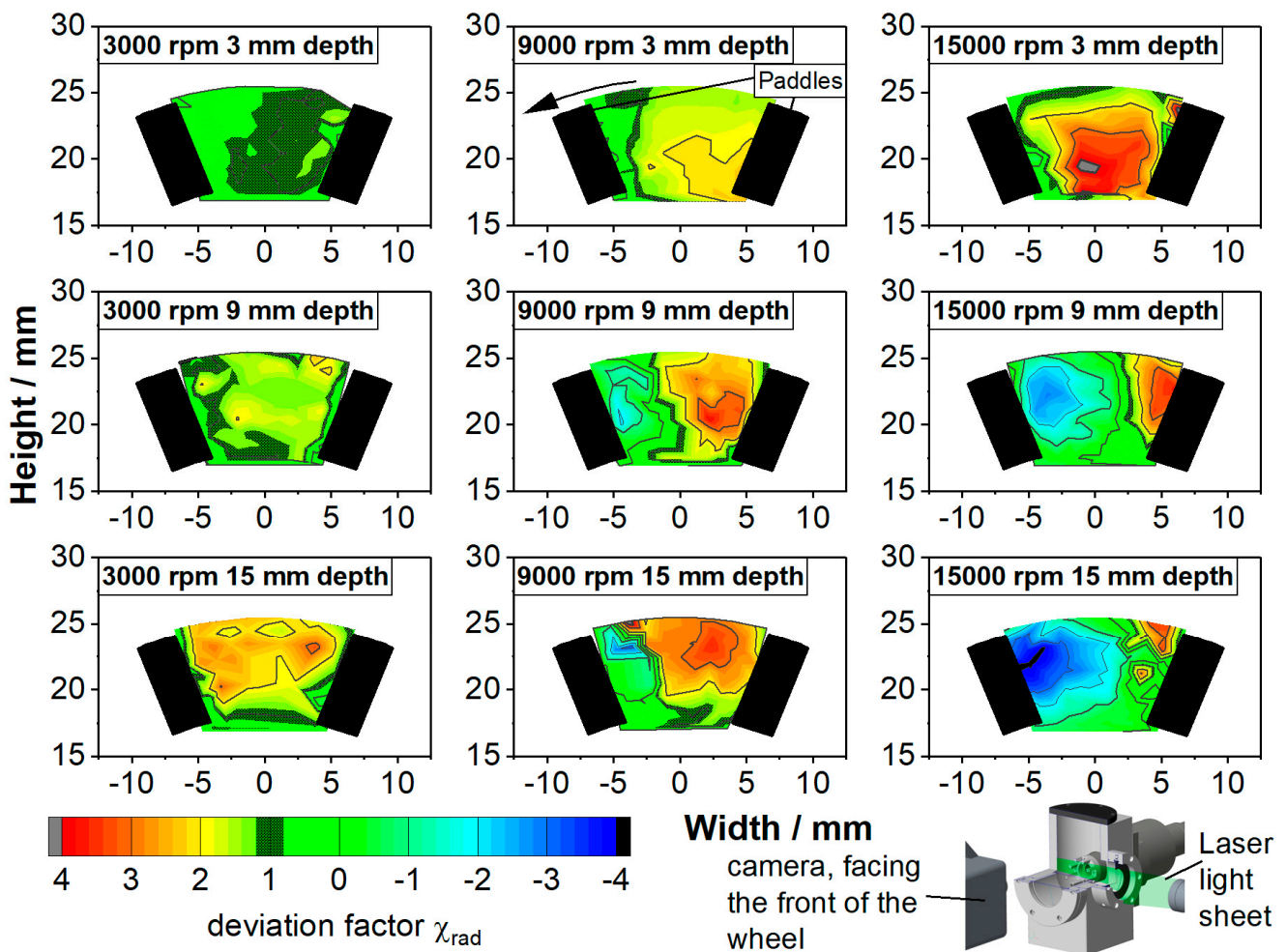
Figure 5. Measured radial air velocity ($v_{rad,meas}$) divided by theoretically assumed, inwardly directed $v_{rad,undisturbed}$ (deviation factor χ_{rad}) at different rotor speeds and depths behind the front glass panel. The black areas indicate the deflector wheel paddles, rotating counterclockwise. In the measurement, the laser light sheet was facing the side, while the camera faced the front. For better visibility, the result was turned by 90°. The black dotted region between the blades indicates a deviation factor of $1 \pm 20\%$, meaning only for this small region the usually assumed radial air velocity approximately equals the air velocity calculated from mass balance and flow-through area.

Additionally, the conservation of angular momentum must also be considered. Because the air in the paddle interspace behaves like a potential vortex, the suction leads the tangential air velocity to surpass the paddle velocity at lower radii (cf. Figure 4). The radial components of this vortex overlay the basic pattern, thus, generating a strongly increased inbound air velocity in front of the trailing paddle and vice versa for the leading paddle.

In other words, the additional vortex behind the leading paddle seems to act as a flow constriction. These vortices were also found in previous work [14,30].

4.2. Impaction Characteristics in Particle-Wall Collisions

Particles with Stokes numbers much greater than one are expected to impact on the deflector wheel paddles during the separation process. To illustrate the process, Figure 6 (left) gives a better overview and is a guide through the following section. The airflow carries particles from the outer region into the zone between the deflector wheel paddles. They can enter the interspace through the whole circumference between the blades and exhibit a certain initial velocity, which is indicated by the small arrows connected to the filled particle. Since the particle's initial velocity is much slower than the circumferential velocity

of the deflector wheel, transposed particle trajectories are shown in the figure so that the deflector wheel paddles appear stationary. The resulting transposed trajectories are shown as dotted lines. The subsequent rebound process can be described by the coefficient of restitution in combination with the scattering of the rebound angle, also called the rebound cone (indicated by the dashed trajectories). Up until this point, particle–particle interactions have been neglected in the schematic overview shown in the figure. They are exemplarily indicated by the hollow particle and might occur at any time.
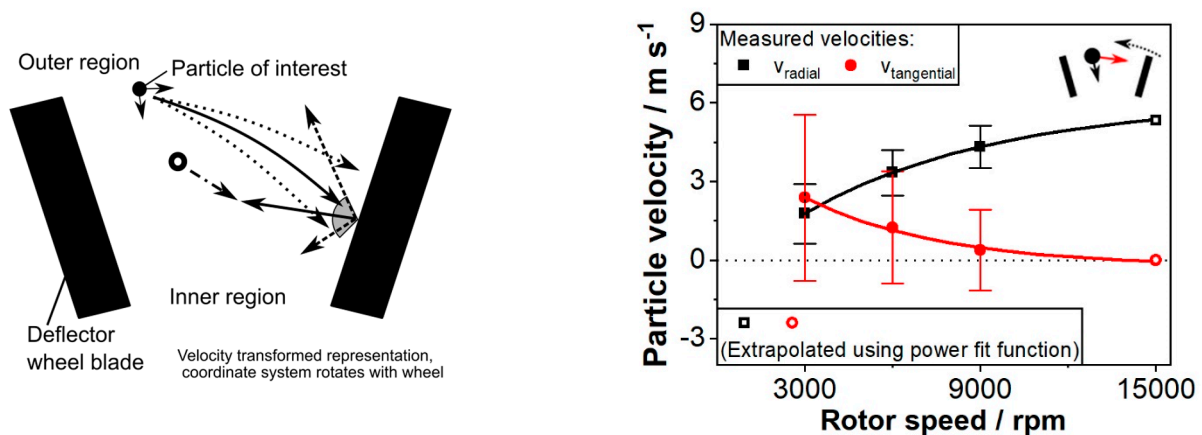
Figure 6. (**Left**) Schematic overview of the particle movement between deflector wheel paddles. A co-rotating representation with the classifier wheel rotating counterclockwise. Interrupted lines represent different alternative trajectories. Collision patterns are more detailed in Section 4.4. (**Right**) Particle motion of limestone particles before impacting on the classifier wheel in a stationary reference frame. For 15,000 rpm, the indicated extrapolated values were used. As indicated in the inlay in the top right corner, positive radial velocities indicate inbound motion (black arrow), while positive tangential velocities indicate clockwise motion (red arrow). The sense of rotation of the deflector wheel is indicated by the dotted black arrow.

Figure 6 (right) shows the measured initial particle velocity of limestone particles before impacting on the deflector wheel paddle for 51 limestone particles per point (error bars indicate the scattering and correspond to plus-minus one standard deviation). Using a high-speed camera and a macro lens, the particle velocity measurement was possible up to rotor speeds of 9000 rpm ($v_{\varphi(ra)}$ = 24 ms^{-1}), while for lower rotor speeds the particles move towards the deflector wheel paddle (positive $v_{tangential}$), the velocity is negligible at increased rotor speeds. However, the radial velocity increases with higher rotor speeds, so that the particles move faster inwards. Overall, the absolute particle velocity, calculated from tangential and radial components only increases by roughly 1 ms^{-1} while the deflector wheel circumferential triples from $v_{\varphi(ra)}$ = 7.9 to 24 ms^{-1}. For 15,000 rpm ($v_{\varphi(ra)}$ = 40 ms^{-1}), the particle's initial velocity is of less significance and, therefore, a simple power fit function was used to estimate the particle velocity to avoid empty data sets in automatic computations.

The comminuted particles are of strongly varying shapes, as shown in Figure 1 (middle and right). As shown in Figure 2, their 2D sphericity comprises the range from Ψ_{2D} = 0.78 (corresponding to equilateral triangle) to Ψ_{2D} = 0.89 (corresponding to squares). In addition, the impaction walls are not smooth but show roughness heights of several 10 microns (cf. Appendix C). In an ideal elastic collision (homogeneous spheres and a smooth wall), the rebound angle of a particle would be equal to the impaction angle (specular rebound). Figure 7 shows probability distributions as a function of the difference between rebound angle and impaction angle of at least 100 particles per case. This difference is nominated as angular imperfection in the following. They were measured with a high-speed camera and a microscopic lens in an impact test bed (particles against a static wall). This setup has the advantage of improved resolution while covering the whole range of impaction

velocities encountered in the deflector wheel classifier. The steel impaction plate was vertically oriented in the measurements of glass spheres and milled glass particles, causing a small bias due to gravity. In all experiments with limestone particles, the impaction plates were horizontal. The slight shift in the mean value of the distribution of limestone particles impacting on the marble plate may be due to the groove profile observed on the marble plate surface (cf. Appendix C). Since surface properties are difficult to control in the experiments, and even more so in actual practice, the interpretation focuses on the width of the distribution.
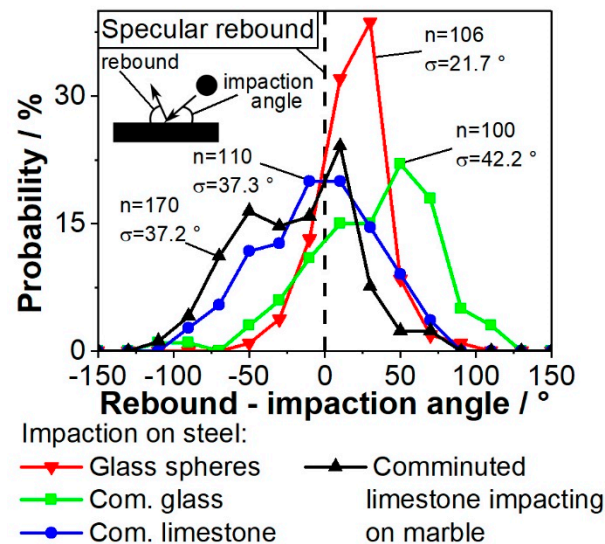
Figure 7. Angular imperfection probability distributions measured in the impact test bed with a microscopic lens for different materials. *n* is the number of evaluated particles and σ is the standard deviation.

For the spherical glass beads, the standard deviation of angular imperfection is 22°, which is attributed to the roughness of the plate, particle rotation, and friction. In contrast, for the non-spherical particles, such as comminuted limestone and comminuted glass particles, the scattering of the angular imperfection is 37° and 42°, respectively. Since the two particulate materials have very different mechanical properties (e.g., Young modulus of limestone: 27.1 GPa and of glass: 70 GPa) but show the same angular imperfection it seems like the impaction with edges and corners is defining the process for the similarly shaped materials (Figure 2, right). This conclusion is supported and extended by the results for limestone particles impacting on the softer marble plate compared to the steel plate (Young modulus 210 GPa) showing nearly the same distribution width.

Figure 8 (left) shows the probability distributions of angular imperfection for at least 50 particles of milled limestone, this time measured with a macro lens directly in the deflector wheel classifier. The mean value of the distributions is shifted towards negative values with increased rotor velocities. This means that the particles are directed less inwardly but more perpendicular forward after the collisions due to the centrifugal force at higher rotor speeds. Another aspect of the particle–paddle collisions in Figure 8 (left) is the reduced scattering with increased rotor speed. For comparison, the results for limestone particles impacting on a static steel plate were grouped into different velocity ranges in Figure 8 (right). Since the number of considered particles was reduced, the distributions are noisier than the data shown in Figure 7. Nevertheless, the probability distributions of the rebound angle minus the impaction angle hardly seem to be affected by the different impact velocities.
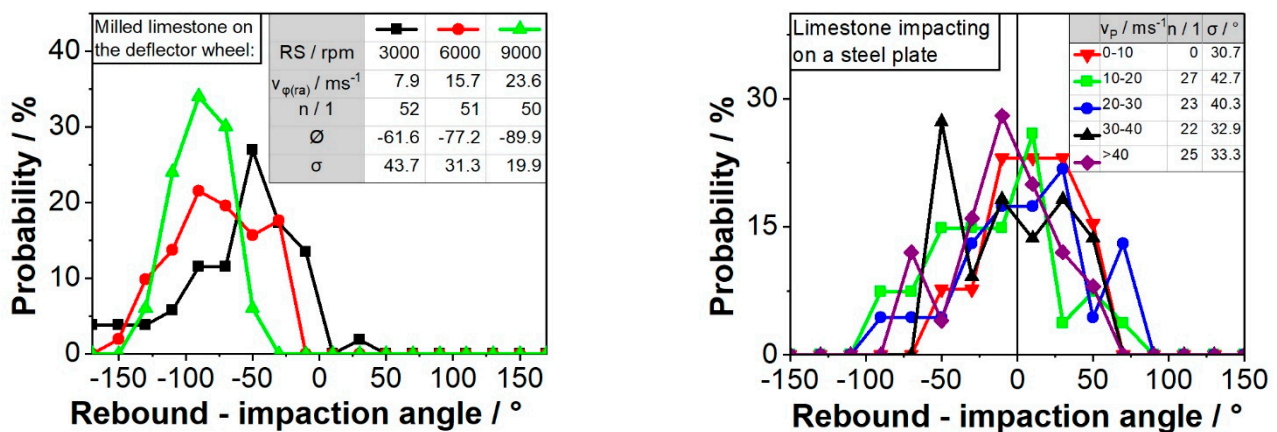
Figure 8. (**Left**) Probability distribution of rebound angle minus impaction angle measured for limestone impacting on the paddles of the aluminum deflector wheel and (**right**) probability distribution of rebound angle minus impaction angle measured for limestone particles impacting on a steel plate in the test bed. RS stands for rotor speed, $v_{\varphi(ra)}$ for the rotor speed at the outer radius, *n* for the number of evaluated particles, Ø for the mean rebound–impaction angle, and σ for the standard deviation.

The reduced scattering of the data in Figure 8 (left) can be explained by a focusing effect of the centrifugal force. Since a smaller magnification was used in the classifier, bigger particles were preferentially evaluated. This unintentional sampling leads to reduced scattering and is not an issue for the microscopic lens in the impact test bed.

Figure 9 shows probability distributions of the normal coefficient of restitution (*COR*). Figure 9 (left) represents the measurement in the deflector wheel classifier for limestone and Figure 9 (right) shows the data measured in the impact test bed for different materials. While the analysis of angles (Figure 8) showed deviating results between the impact test bed and the classifier, the coefficient of restitution shows few discrepancies. For limestone impacting on the steel plate in the impact test bed and on the aluminum deflector wheel, the mean coefficient of restitution is almost identical. Figure 9 (left) shows a minimal influence of the rotor speed, but considering the variation between single-particle measurements, the difference of 0.05 in the mean value is negligibly small.

In Figure 9, the predicted *COR* for spherical particles using the model of Thornton [24,25] for elastic-plastic deformation during collision and the literature material properties is shown (bars in the top). The right edge of the colored area is for $1~\text{ms}^{-1}$ impaction velocity and the left side for $40~\text{ms}^{-1}$. This estimation gives an overview of the *COR* values expected to occur for spherical particles and a smooth wall.

While the glass beads show the expected high *COR*, approximately between 0.7 and 0.8, the comminuted glass exhibits a significantly reduced *COR*. Interestingly, minimal differences between comminuted limestone particles or comminuted glass particles impacting on the steel plate were found in the measurements.

Additionally, a split-up of the data in velocity ranges (like the one in Figure 8, right) did not show a velocity dependence within the studied range. The differences due to irregular shape and wall roughness are more significant than the differences due to impaction speed. Thus, these findings can be summarized by saying that even though the mechanical properties varied significantly, the particle rebound behavior was very similar with a similar shape.
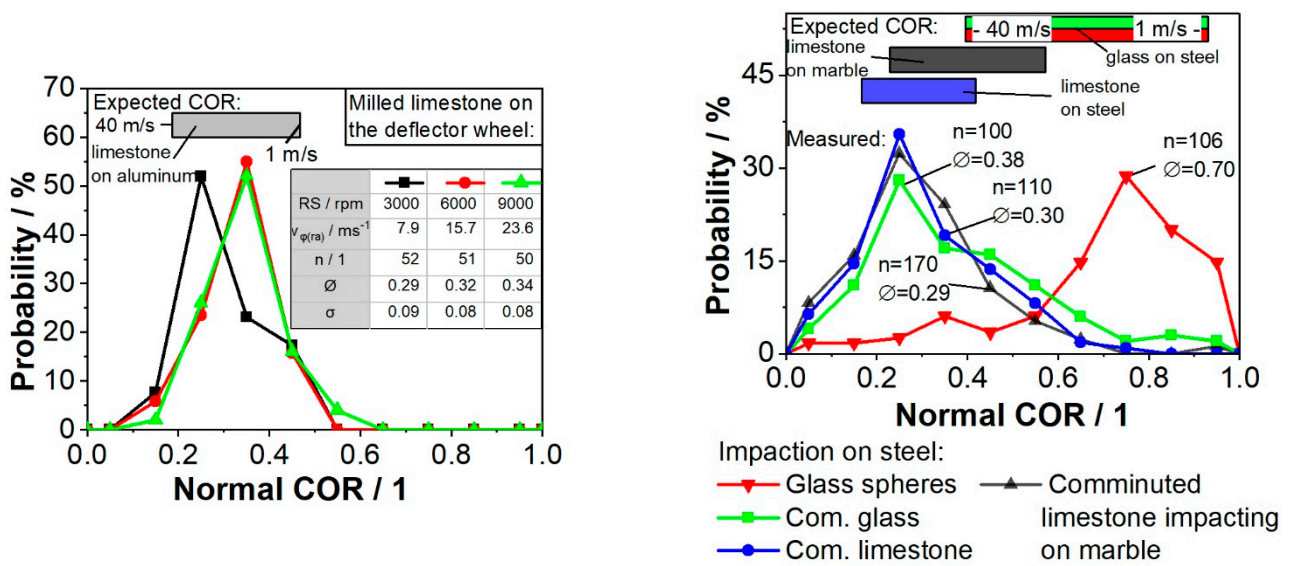
Figure 9. Normal coefficient of restitution (COR) probability distribution. (**Left**) measured in the deflector wheel classifier for limestone particles and (**right**) measured in the impact test bed for different materials. The colored bars on the top shows the range of the expected values for spherical particles impacting on a smooth wall predicted by the model of Thornton [24,25] and the literature material properties for 1 m/s to 40 m/s. RS stands for rotor speed, $v_{\varphi(ra)}$ for the rotor speed at the outer radius, *n* for the number of evaluated particles, Ø for the mean COR, and σ for the standard deviation.

The coarse particle behavior shown in Figure 6 (left) serves as the foundation of the model presented in detail below: The particles enter the deflector wheel interspace over the entire free circumference with the velocity distribution determined in Figure 6 (right). During the approach phase, drag is neglected in the model and, thus, the impaction radius, impaction velocity, and impaction angle distributions can be calculated.

Figure 10 compares the calculated impaction distributions from DEM simulations, where the airflow affects the particle trajectory during the approach phase, with the model calculations, where the particle movement is not affected by the airflow during the approach phase. Furthermore, the experimentally determined so-called impaction length, measured by Spötter et al. [30], is depicted in the figure as a dashed vertical line. This parameter specifies the smallest radius at which the particles impacted the paddle during the experiments. The green bars represent the overlap of the probabilities calculated by DEM and the model approach. The part that is only filled by DEM is shown in red, and the part that only the model fills is shown in blue. The radial extent of the DEM simulation data matches the experimentally determined values from Spötter et al. [30] very well. However, the influence of air during the approach phase is almost negligible, for the particles used here with high Stokes numbers (≥20) (difference between the blue + green and the red + green bars).
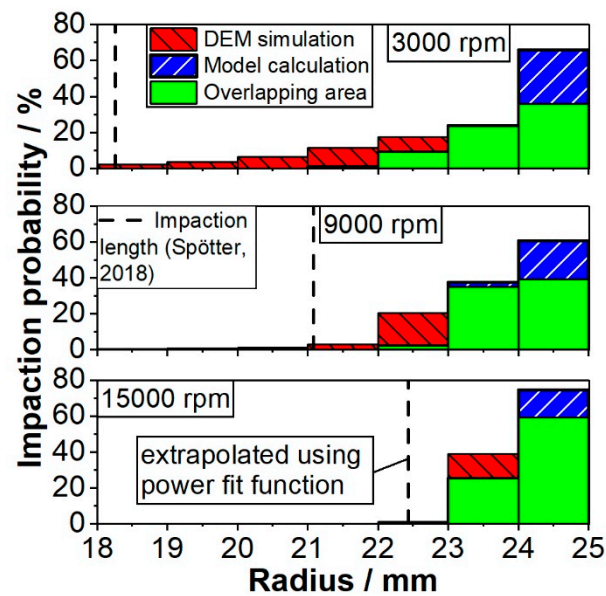
Figure 10. Impaction probability versus radius calculated in DEM simulations with the influence of drag, calculated in the model without the influence of drag, and the impaction length measured by Spötter et al. [30].

4.3. Particle–Particle Interactions

For many particulate systems, it is difficult to determine particle–particle interactions experimentally. Strobel et al. [33], however, used malleable particles in a mill to record their deformation from the process by analysis of SEM pictures before and after the process. From the number and area of the observed dents, they deduced the number and intensity of particle–particle collisions. In our case, the particles form a constant hold-up in the classifier casing [27] and reach the deflector wheel multiple times; therefore, this method is not suitable here. Another possibility is to simulate the multiphase flow numerically, as Toneva et al. [12,13] did for a different kind of deflector wheel classifier with a mass loading of 0.1 kg (particles) kg (air)$^{-1}$ [13]. However, the high mass loading in the hold-up of this system still creates a problem because approximately 2×10^{11} [27] particles are kept in the peripheral region of the deflector wheel ($\approx$1.6 L) and it takes up to 1 h to reach stationary conditions [4].

DEM simulations described in Section 3.5 were performed using one paddle interspace to overcome this issue. The actual mass loading in the hold-up of approximately 40 kg (particles)/kg (air), reported in [27], was used as the particle mass inflow condition to generate the particles randomly over the entire circumferential area of the outer region of the paddle interspace. Weers et al. [27] found this loading to be independent of the feed rate, while Spötter et al. [30] found that for this deflector wheel classifier, the actual feed rate had a minor influence on the separation efficiency.

In addition to ideal spherical particles, brick-shaped polyhedra are generated to analyze the influence of the particle shape. The polyhedra are meant to share the mean 3D sphericity of the comminuted limestone particles in Figure 2 (right), which leads to its dimensions of a = b and c = 2.08a. The size distribution of Saxolith 70, from Figure 2 (left), is used for both the spherical and polyhedral particles, and the particle density is set to $\rho_P = 2700$ kgm^{-3}. The initial particle velocities were randomly set in the range of the observed particle movement of limestone particles before impact on the classifier wheel (Figure 6, right). In addition, the coefficients of the linear spring-damper model for the polyhedra particles were adjusted so that the computed mean restitution coefficient matches the observed one. The measured flow from Section 4.1 was transferred to the simulation model for the respective rotor speeds to generate the stationary flow field. For this purpose, the flow data in 3 mm, 9 mm, and 15 mm depths were inter- and extrapolated to a three-

dimensional cartesian mesh with 50,000 cells in the range of depths from 0–18 mm. For this reason, the geometry of the paddle interspace has also been cut to a depth of 18 mm. The DEM time step is set to 4×10^{-10} s to ensure that the particle contacts of the smallest particles are resolved as fine enough, and the total simulation time is 0.05 s.

Figure 11 displays the mean number of particle–particle collisions for the rotor speeds of 3000 rpm, 9000 rpm, and 15,000 rpm. The left-hand side shows the shape of the probability distributions for non-spherical particles with a low coefficient of restitution and spherical particles with a high coefficient of restitution, while the right-hand side summarizes the data in mean values and standard deviations. According to these simulations, spherical particles exhibit approximately one-fifth of the particle interactions of non-spherical particles and exhibit a significantly reduced standard deviation. The number of particle–particle collisions seems to correlate with the time close to the deflector wheel paddle since the spherical particles with a high *COR* show the lowest number of interactions, followed by the spheres with a lower *COR*. On the other hand, the polyhedra impacted with edges and corners and showed significantly more rotary momentum during the simulations, leading to a prolonged stay between the paddles. Regarding particle size and calculated residence time in the paddle interspace, no dependencies could be found due to the domination of scattering.
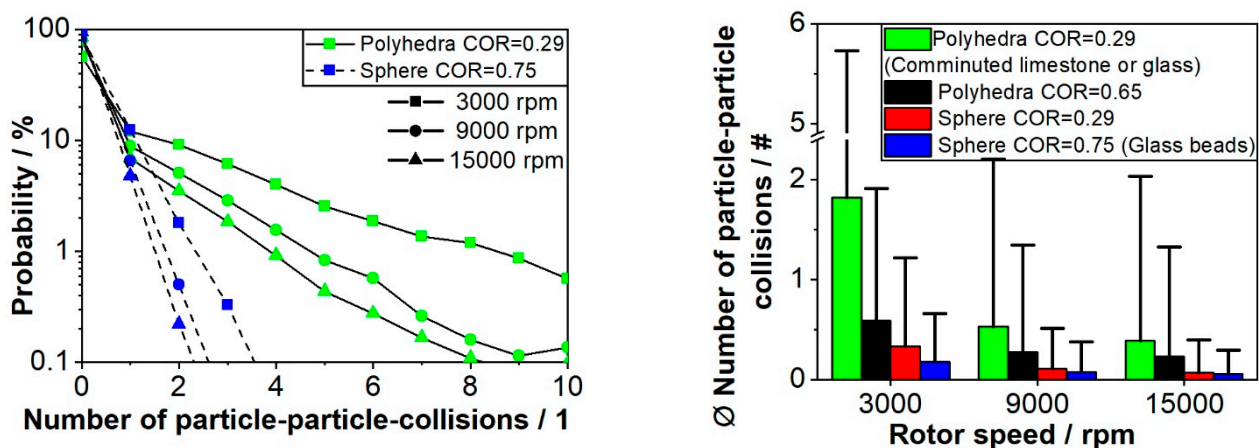

Figure 11. Simulation results regarding the particle–particle-collisions in the deflector wheel classifier for spherical and non-spherical particles at different rotor speeds. (**Left**) shows the probability distribution of the number of contacts for polyhedral particles with a low coefficient of restitution (comminuted limestone or glass) and spheres with a high coefficient of restitution (glass beads). This is the probability that a particle has 0, 1, . . . particle–particle-collisions in the paddle interspace; (**Right**) Mean number of particle–particle interactions plus one standard deviation occurring on the path from inlet to outlet surface.

To summarize, the DEM simulation determined the number of particle–particle collisions in the classifier wheel interspace. Because the same loading in the hold-up was discovered at different feed rates, these apply to the various operating conditions [27]. However, in a simple model, it is still not possible to directly convert the collision numbers determined by DEM into particle motions. As a result, a theoretical consideration is established for the model, and the used approach is based on the distinction of three possibilities: (1) a particle can collide with the classifier wheel blade unaffected, (2) accelerate another particle after colliding with the blade and then be hit by the classifier wheel again, or (3) be the particle accelerated by another particle. Section 4.4 contains a more detailed description of this method. The DEM provided the weighting for the various cases and the tromp curves (T) were calculated as a function of the number of particle–particle-collisions (*n*) indicated in Figure 11 (left).

4.4. Model to Predict the Separation Characteristics of a Deflector Wheel Classifier

Because the theoretical and experimental cut sizes differ significantly when the simple model in Equation (3) or Equation (6) is used (cf. Figure 13) with the usual assumptions, the goal of this work is to predict the cut size and separation sharpness from easily measurable data in order to gain a better understanding of the separation process and to refine the assumptions. If the material properties can be appropriately differentiated from the machine properties, the separation process can be predicted, reducing experimental effort and, thus, costs.

Here, the developed model is still based on Equation (6) but uses refined input values/distributions. The four key parameters are particle tangential velocity, radial air velocity, drag coefficient, and particle sphericity. The following model description begins by determining a particle tangential velocity distribution, followed by the other three more straightforward or already determined values. Using the measured distributions, cumulative cut size distributions are calculated, corresponding to the experimental separation curves.

First, the model uses the initial particle velocity distributions from Figure 6 (right) to calculate the trajectory of the particle and determine the impaction angle, impaction velocity, and impaction radius distributions for the unaffected particles. This was previously described in detail in Section 4.2.

On the other hand, the particle–particle interactions are a rather complex topic that needs DEM simulations and a supercomputer system to be solvable. The goal of the presented model is to reduce this effort so that a calculation using a personal computer is possible. To solve this, a hypothetical case distinction is made here: A fraction of the particles can impact on the deflector wheel classifier blade relatively unaffected by other particles. This would correspond to Case A in Figure 12. The particle could, for instance, not interact with another particle during the classification process or only with a particle that exhibits roughly the same velocity and direction. The latter would be the case if both particles were on their way to the deflector wheel paddle, or both were already accelerated. For Case A, the tangential particle velocity distribution after the deflector wheel contact is calculated by combining the aforementioned distributions with the COR distribution (Figure 9, right) and angular imperfection distribution (Figure 7) as determined by Figure 11 (left), which holds for most particles.

For particles that interact with other particles, two additional and more theoretical cases can be derived: Case B and C of Figure 12. Here, two particles interact with counter-directed velocities. The first particle, already accelerated by the deflector wheel, transmits its velocity to an incoming particle that is on its way to the deflector wheel paddle. Regarding the situation after particle–particle collision, the accelerated particle corresponds to Case B, while the decelerated particle corresponds to Case C. The contact partners were assumed to have the same mass. For particle–wall collisions, Wu et al. [23,34] found that the rebound behavior significantly changed from deformation to sliding if the impact angle between the trajectory and the wall is below between 25 and 35° (65–55° from the perpendicular axis). As an extrapolation for the particle–particle collision, the rebound trajectory for the particle of Case B is equally distributed in an opening cone with an angle of 130° (65° from the perpendicular axis for each side). In this case, sliding would lead both particles to spin, which was neglected, instead of rebounding in a certain direction.

Using this approach and a mean particle–particle COR from Figure 9 (right), the particle tangential velocity distribution can be calculated for Case B.

The decelerated particle (Case C), on the other hand, collides with its new impaction velocity distribution and an undetermined impaction radius on the deflector wheel classifier paddle. Here, a 90° impaction angle and the impaction radius distribution from Figure 10 are assumed. The tangential rebound velocity of this particle is then calculated in the same manner as for the unaffected particle. The dominating aspect of multiple particle–particle contacts is whether a particle was "approximately unaffected" (Case A), "re-accelerated by the deflector wheel" (Case B), or "accelerated by another particle" (Case C). Even for

this simple approach with its vast assumptions, it is rather difficult to estimate how often the single cases might occur. The procedure for the estimation is presented using one particle–particle interaction (Figure 12, table a) as a set value. The maximum number of interactions for the particle of interest is equal to 2 n + 1, where *n* is the set number of particle–particle collisions. In the example, the particle can experience a maximum of three collisions, during which it is alternately accelerated and decelerated.
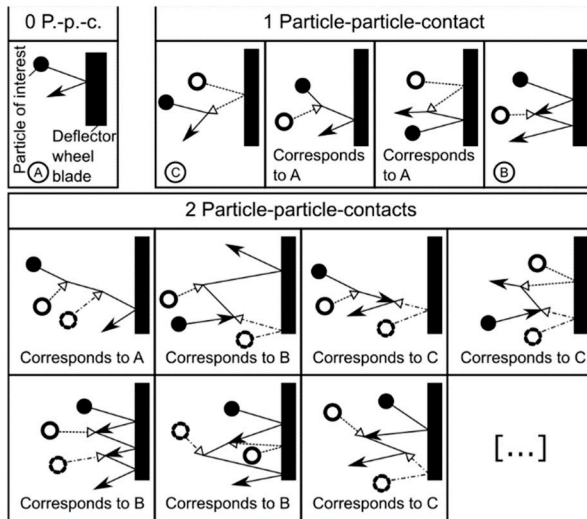
(a) For 1 particle-particle contact

Collision A	Collision B	Collision C	↑ In binary ↑	Collision A	Collision B	Collision C
	P			+1	-1	+1
	P	W		+1	+1	-1
W	P			-1	+1	+1
W	P	W		-1	-1	-1

(b)

Number of particle-particle contacts	Probability of Case A/1	Probability of Case B/1	Probability of Case C/1
0	1/1	-	-
1	2/4	1/4	1/4
2	3/12	3/12	6/12
3	4/36	9/36	23/36

Figure 12. Theoretical classification of particle–wall and particle–particle interactions for 0, 1, and 2 particle–particle contacts (P.-p.-c.). Table a shows the conversion from particle–deflector wheel paddle collision (W) and particle–particle collision (P), exemplary for one particle–particle contact. Table b lists the probabilities for Cases A, B, and C calculated by permutation and filtering of unrealistic combinations.

The acceleration and deceleration can be put into a binary system (Figure 12, table a), where the particle–deflector wheel paddle collision (W), reversing the particle's direction of movement, is set to (−1), and the particle–particle collision (P) is either counter directed (−1) or in an aligned direction (+1). If the particle does not interact with the classifier wheel, the value is set to neutral (+1). The permutation of three binary variables results in six possibilities (factorial of 3), but the table consists of only four possibilities since the particle impacting on the blade then colliding with a similar directed particle to finally impacting on the wheel again is not sound. After clearing the matrix from similar cases, one can derive the probabilities for Case A, B, and C for any set number of particle–particle collisions by permutation and filtering out impossible combinations (Figure 12, table b). Additionally, the chance of a particle from Case C re-impacting on the deflector wheel paddle was neglected during this estimation.

In summary, the particle tangential velocity distributions for Cases A, B, and C, as well as associated impaction radius distributions were estimated.

To calculate cut particle sizes (Equation (6)), the radial air velocity at the various radii is calculated using radial deviation factors (from Figure 5) of 2.7, 4.1, and 4.3 for 3000, 9000, and 15,000 rpm, respectively. For the drag coefficient, the measured 2D sphericity (Figure 2, right) is converted to a 3D sphericity using Equation (5), which is then entered in Equation (4) as Ψ_{3D} and $\Psi_{\perp,\parallel}$ since no alignment effects or pronounced length to diameter ratios (like in fibers) occur. Because the flow regime is in the transition regime ($5 \leq Re \leq 90$), the drag coefficient (Equation (4)) is determined iteratively.

Finally, Cases A, B, and C are weighted according to Figure 12, table b, and the calculated cut size distributions for 0, 1, 2, (…) particle–particle interactions are weighted

concerning the number of particle–particle collisions determined by DEM (Figure 11, left). This yields a cumulative cut particle size distribution corresponding to a separation curve.

In the top part of Figure 13a, the experimentally determined separation curves for limestone are shown and compared to the predicted ones by the model. The calculated tromp curve is in acceptable agreement with the experimentally obtained separation curves. Appendix E shows the experimental cut sizes compared to the not-weighted separation curves of the model for 0, 1, and 2 particle–particle contacts during the separation process to show the difference if no DEM were performed or the effective mass load changed. In Figure 13 the model-based separation efficiency curve was mostly steeper than the experimentally determined one. Since the particle inlet to the classification chamber (cf. Figure 3) is below the deflector wheel, and the deflected material passes this inlet on its way to the coarse material outlet, some mixing might occur with part of the feed material going straight into the outlet. Additionally, insufficient dispersing due to high cohesion forces has to be expected for fine particles since the classifier does not have a dedicated dispersing unit. Both effects, i.e., mixing and cohesion, will enhance the fine fraction included in the coarse product.
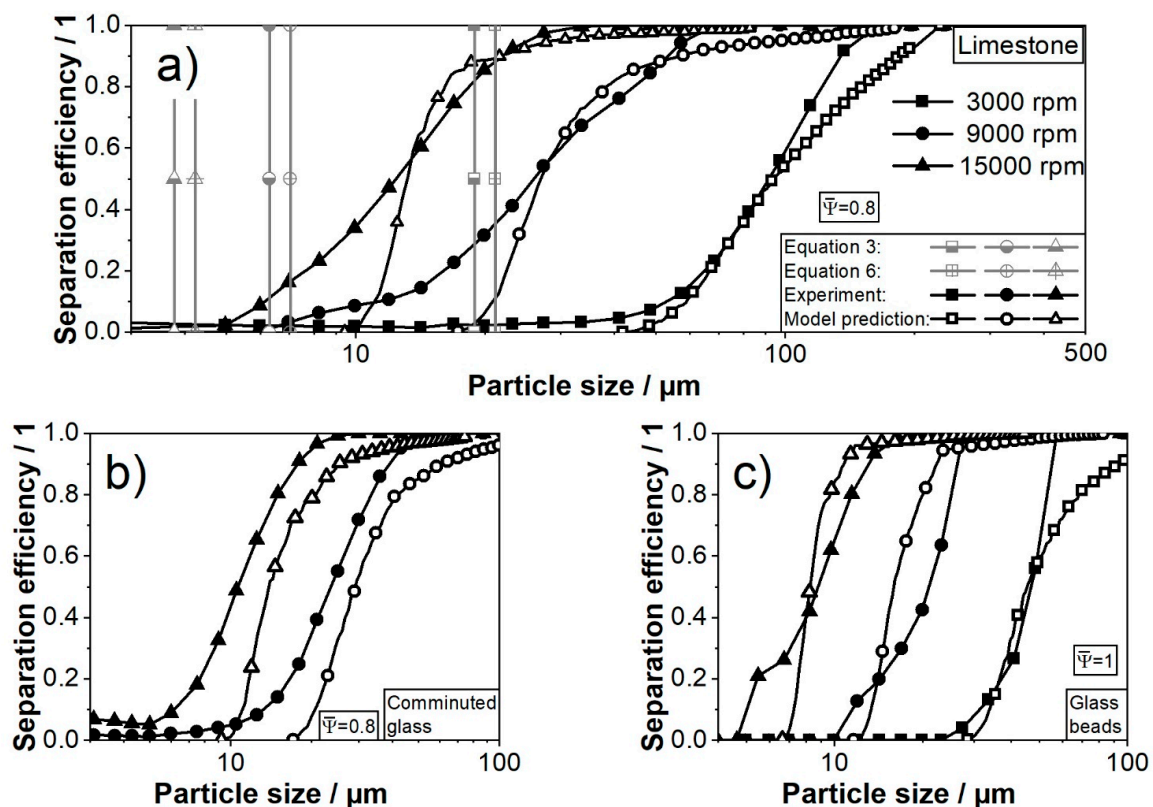

Figure 13. Experimentally measured separation curves versus the cut particle size calculated using Equations (3) and (6) and model predictions using the number of contacts (Figure 10) from DEM simulations. (**a**) is for limestone with $\overline{\psi}$ as used in 2D sphericity for the calculations; (**b**) shows the result for comminuted glass and (**c**) for glass beads.

Figure 13b shows the experimental and predicted separation curves for comminuted glass particles. The curves are only given for 9000 rpm and 15,000 rpm since the material was too fine to be separated at 3000 rpm. The same deviation factor as for the limestone predictions was used for these calculations and the increased number of particle–particle contacts from DEM simulations. The predicted and experimental curves are very similar, with the experimental one being slightly offset to fine.

Figure 13c shows the separation efficiency curve for glass beads determined by experiments and predicted using the presented model. Again, a minor offset can be found, while

the curve course fits well. In contrast to the investigations using comminuted glass, the offset of the model is shifted towards fine here. Since the starting velocity (how particles enter the blade interspace) was only measured for the limestone particles, both deviations mentioned above might be attributed to particle-dependent inlet conditions. It was demonstrated that an acceptable separation efficiency prediction is possible, using the measurable variables regarding the material impaction characteristics from an impaction test bed, the particle shape, the deflector wheel classifier flow field, and the number of particle–particle interactions.

5. Conclusions

Even though the basic separation principle of deflector classifiers has been known and used for a long time, the prediction of the separation curve with sufficient accuracy is still a challenge. The underlying influencing parameters are only considered and incorporated to a limited extent. Therefore, all steps of the separation process are considered here, including gas flow patterns within the paddles of the deflector wheel, particle trajectories in the approach and rebounding phase, particle–wall and particle–particle collisions, and finally, the balance between centrifugal and drag force.

The airflow was measured using a PIV system. While the tangential air velocity in the interspace of the paddles was similar to the deflector wheel circumferential velocity, the radial air velocity showed significant differences compared to the calculation from mass balance and flow-through area. The formation of so-called channel vortices led to velocities up to 4x the expected radial air velocity in the region close to the tailing paddle.

In this work, the particle–wall interactions were investigated using a high-speed camera along with an impaction test bed and the classifier. It was found that comminuted glass behaves like the much softer comminuted limestone in the impaction test bed and during the separation, unlike glass beads. The particle sphericity, determined with dynamic image analysis, showed a tetrahedral or cubic shape for both comminuted particle systems and the effect of the particles impacting on edges and corners seemed to dominate the rebound behavior more than the mechanical properties.

Using these aspects, the particle velocity at the entrance between the paddles and the effective mass loading, DEM simulations could determine the number of particle–particle interactions during the separation process. The number of particle–particle contacts seemed to correlate with the particle shape and COR.

The presented model considered all the previously stated aspects and estimated single-particle deflection probabilities using the different probability distributions. For limestone, the separation curves could be predicted very well, while glass beads and comminuted glass showed systematic differences, which can be eliminated by calibration. Only one experiment would suffice to determine the offset of the parameters and to extrapolate to different rotor speeds. Future work could focus on the scalability for materials with a different density such as lightweight fillers or metal alloys and a differently dimensioned classifier wheel.

Appendix A. Setup of the PIV System and a Picture of the Evaluation
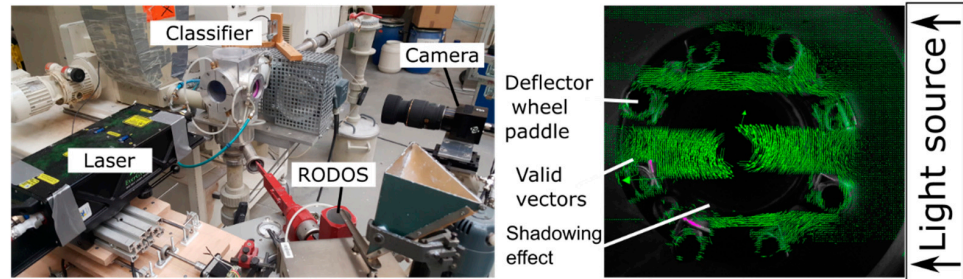

Figure A1. (**Left**) Shows the experimental PIV setup with the camera facing the side of the classifier wheel and the laser facing the front. (**Right**) Shows a picture of the evaluation with an unprocessed photograph in the background and a reduced number of valid vectors for improved visibility.

Appendix B. Superimposed Picture of the Impaction Process
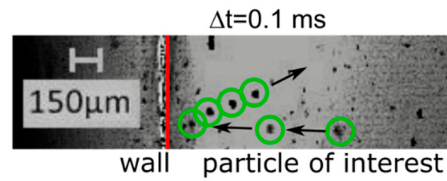

Figure A2. Superimposed picture of a limestone particle, impacting on the steel wall in the impact test bed. The measurement was conducted with 230,000 fps and the chosen time interval between each of the superimposed pictures (green circles) is 0.1 ms.

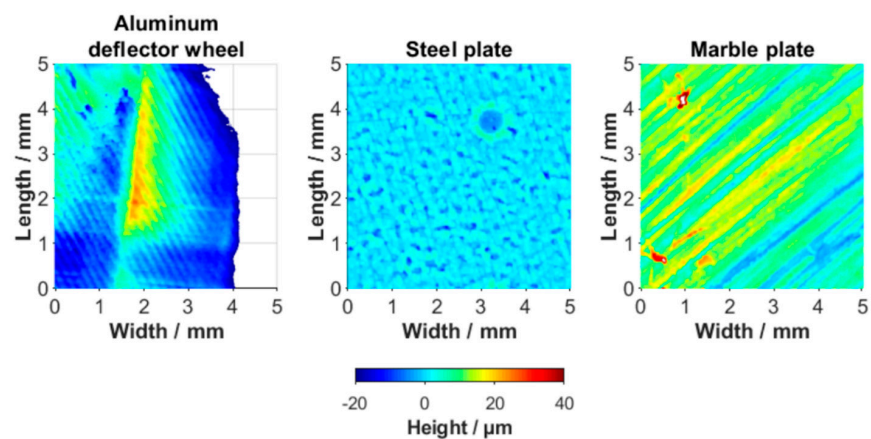## Appendix C. Surface Profiles of the Different Wall Materials

Figure A3. Surface height profile of the used impaction plates, measured with a white light interferometer (Sensor: WLI PL, FRT GmbH).

Appendix D. Numerical Setup—Particle, Wall, and Interaction Properties

Table A1. Additional parameters set in the DEM simulations.

Particle size distribution	1–180 μm, corresponding to Saxolith 70
Mass inflow	40 kg/kg(air)
Dimensions polyhedral	A = b; c = 2.08a
Particle density ρ_P	2700 kg/m^3
Average restitution coefficient e	0.29; 0.65; 0.75
Friction coefficient μ_c	0.8
Stiffness ratio k^t/k^n (n = normal, t = tangential)	0.86 (Particle-Particle); 0.78 (Particle-Wall)
Collision time t^n	1×10^{-8} s
DEM time step t_{DEM}	4×10^{-10} s
Interpolated mesh [-]	50,000 cells
Simulated time	0.05 s

Appendix E. Experimental and Model Separation Curves for 0, 1, and 2 Particle–Particle Contacts
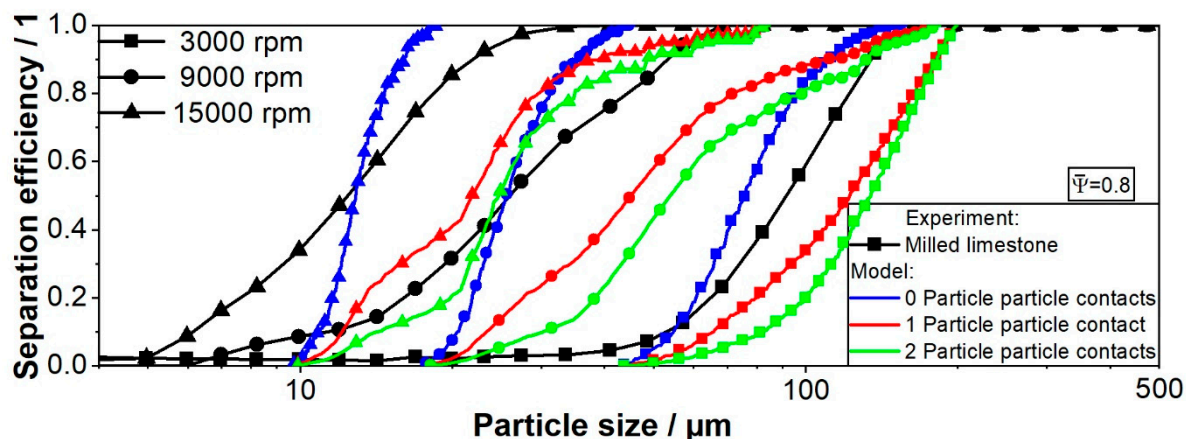

Figure A4. Experimental separation curves compared to the model predictions of 0, 1, and 2 particle–particle contacts during the separation process for limestone. This was calculated by weighting Cases A, B, and C according to Figure 12, right (neglecting the weighting from Figure 11, left) to show the range of the results if no DEM simulations were performed.

References

1. Rumpf, H.; Raasch, J. *Desagglomeration in Stroemungen, Symposium "Zerkleinern" Frankfurt am Main*; Verlag Chemie: Weinheim, Germany, 1962.
2. Galk, J. *Feinsttrennung in Abweiseradsichtern*; Technische Universität Clausthal, Botermann&Botermann Verlag: Köln, Germany, 1995.
3. Bauer, U. *Zur Trennscharfen Feinstsichtung in Fliehkraft-Abweiseradsichtern*; Technische Universität Clausthal, Shaker-Verlag: Aachen, Germany, 2002.
4. Spötter, C. Dynamik der Trenncharakteristik eines Abweiseradsichters. Ph.D. Thesis, TU-Clausthal, Papierflieger-Verlag, Clausthal-Zellerfeld, Germany, 2018.
5. Rumpf, H.; Leschonski, K. Prinzipien und neuere Verfahren der Windsichtung. *Chem. Ing. Tech.* **1967**, *21*, 1231–1241. [CrossRef]
6. Rumpf, H.; Sommer, K.; Stieß, M. Berechnung von Trennkurven für Gleichgewichtssichter. *Verfahrenstechnik* **1974**, *8*, 261–263.
7. Molerus, O. Stochastisches Modell der Gleichgewichtssichtung. *Chem. Ing. Tech.* **1967**, *13*, 792–796. [CrossRef]
8. Molerus, O.; Hoffmann, H. Darstellung von Windsichtertrennkurven durch ein stochastisches Modell. *Chem. Ing. Tech.* **1969**, *5–6*, 340–344. [CrossRef]
9. Schubert, H. *Aufbereitung Fester Mineralischer Rohstoffe—Band 1*; Deutscher Verlag für Grundstoffindustrie: Leipzig, Germany, 1968.
10. Husemann, K. Modellierung des Sichtprozesses am Abweiserrad/Modelling of a Classifying Process Using a Deflecting Wheel. *Aufbereitungstechnik* **1990**, *31*, 359–366.
11. Legenhausen, K. Untersuchung der Strömungsverhältnisse in Einem Abweiseradsichter. Ph.D. Thesis, TU Clausthal, Clausthal-Zellerfeld, Germany, 1991.

12. Toneva, P.; Epple, P.; Breuer, M.; Peukert, W.; Wirth, K.E. Grinding in an air classifier mill—Part I: Characterisation of the one-phase flow. *Powder Technol.* **2011**, *211*, 19–27. [CrossRef]

13. Toneva, P.; Wirth, K.E.; Peukert, W. Grinding in an air classifier mill—Part II: Characterisation of the two-phase flow. *Powder Technol.* **2011**, *211*, 28–37. [CrossRef]

14. Stender, M.; Legenhausen, K.; Weber, A.P. Visualisierung der Partikelbewegung in einem Abweiseradsichter. *Chem. Ing. Tech.* **2015**, *87*, 1392–1401. [CrossRef]

15. Spötter, C.; Legenhausen, K.; Weber, A.P. Einfluss der Sichtradgeometrie auf die Sichtluftströmung und Partikelbewegung eines Abweiseradsichters. *Chem. Ing. Tech.* **2018**, *4*, 493–506. [CrossRef]

16. Spötter, C.; Elskamp, F.; Hennig, M.; Teipel, U.; Weber, A.P.; Kruggel-Emden, H. Trennkurven in Siebung und Gegenstromsichtung bei geringen Gutbeladungen. *Chem. Ing. Tech.* **2017**, *89*, 1726–1738. [CrossRef]

17. Furchner, B.; Zampini, S. Air Classifying. Ullmann's Encycl. *Ind. Chem.* **2012**, *2*, 215–234. [CrossRef]

18. Nied, R. Fine classification with vaned rotors: At the outer edge of the vanes or in the interior vane free area? *Int. J. Miner. Process.* **2004**, *74*, 137–145. [CrossRef]

19. Rorato, R.; Arroyo, M.; Andò, E.; Gens, A. Sphericity measures of sand grains. *Eng. Geol.* **2019**, *254*, 43–53. [CrossRef]

20. Hölzer, A.; Sommerfeld, M. New simple correlation formula for the drag coefficient of non-spherical particles. *Powder Technol.* **2008**, *184*, 361–365. [CrossRef]

21. Ahmad, M.; Ismail, K.A.; Mat, F. Impact models and coefficient of restitution: A review. *ARPN J. Eng. Appl. Sci.* **2016**, *11*, 6549–6555.

22. Tomar, V.; Bose, M. Anomalies in normal and oblique collision properties of spherical particles. *Powder Technol.* **2018**, *325*, 669–677. [CrossRef]

23. Kleinhans, U.; Wieland, C.; Frandsen, F.J.; Spliethoff, H. Ash formation and deposition in coal and biomass fired combustion systems: Progress and challenges in the field of ash particle sticking and rebound behavior. *Prog. Energy Combust. Sci.* **2018**, *68*, 65–168. [CrossRef]

24. Thornton, C.; Ning, Z. A theoretical model for the sick / bounce behaviour of adhesive, elastic-plastic spheres. *Powder Technol.* **1998**, *99*, 154–162. [CrossRef]

25. Thornton, C.; Cummins, S.J.; Cleary, P.W. On elastic-plastic normal contact force models, with and without adhesion. *Powder Technol.* **2017**, *315*, 339–346. [CrossRef]

26. Hinds, W.C. *Aerosol Technology*, 2nd ed.; John Wiley & Sons, Inc.: Los Angeles, CA, USA, 1999; ISBN 0-471-19410-7.

27. Weers, M.; Wollmann, A.; Teipel, U.; Weber, A.P. Dynamics of Separation Characteristics of Sieving and Flow Classification Processes. In *Dynamic Flowsheet Simulation of Solids Processes*; Heinrich, S., Ed.; Springer Nature: Berlin, Germany, 2020.

28. Di Felice, R. The voidage function for fluid-particle interaction systems. *Int. J. Multiph. Flow* **1994**, *20*, 153–159. [CrossRef]

29. Vollmari, K.; Jasevičius, R.; Kruggel-Emden, H. Experimental and numerical study of fluidization and pressure drop of spherical and non-spherical particles in a model scale fluidized bed. *Powder Technol.* **2016**, *291*, 506–521. [CrossRef]

30. Spötter, C.; Legenhausen, K.; Weber, A.P. Separation Characteristics of a Deflector Wheel Classifier in Stationary Conditions and at High Loadings: New Insights by Flow Visualization. *KONA Powder Part. J.* **2018**, *35*, 172–185. [CrossRef]

31. Xing, W.; Wang, Y.; Zhang, Y.; Yamane, Y.; Saga, M.; Lu, J.; Zhang, H.; Jin, Y. Experimental study on velocity field between two adjacent blades and gas-solid separation of a turbo air classifier. *Powder Technol.* **2015**, *286*, 240–245. [CrossRef]

32. Sun, Z.; Sun, G.; Liu, J.; Yang, X. CFD simulation and optimization of the flow field in horizontal turbo air classifiers. *Adv. Powder Technol.* **2017**, *28*, 1474–1485. [CrossRef]

33. Strobel, A.; Romeis, S.; Wittpahl, S.; Herre, P.; Schmidt, J.; Peukert, W. Characterization of stressing conditions in mills—A comprehensive research strategy based on well-characterized model particles. *Powder Technol.* **2017**, *305*, 652–661. [CrossRef]

34. Wu, C.-Y.; Thornton, C.; Li, L.-Y. Coefficients of restitution for elastoplastic oblique impacts. *Adv. Powder Technol.* **2003**, *14*, 435–448. [CrossRef]